Newtonian fluid flow through Microfabricated Hyperbolic Contractions

Mónica S. Neves Oliveira[1, 2], Manuel A. Alves[1],

Fernando T. Pinho[3, 4], Gareth H. McKinley[2]

1: Departamento de Engenharia Química, CEFT, Faculdade de Engenharia da Universidade do Porto, Porto, Portugal, monica.oliveira@fe.up.pt, mmalves@fe.up.pt

2: Department of Mechanical Engineering, Massachusetts Institute of Technology, Cambridge MA 02139, USA, gareth@mit.edu

3: CEFT, Faculdade de Engenharia da Universidade do Porto, Porto, Portugal, fpinho@fe.up.pt

4: Universidade do Minho, Braga, Portugal, fpinho@dem.uminho.pt

Abstract

We study the flow of a Newtonian fluid through microfabricated hyperbolic contractions in detail. A set of planar converging geometries, with total Hencky strains ranging from 1 to 3.7, have been fabricated in order to produce a homogeneous extensional flow field within the contraction. The kinematics in the contraction region are investigated experimentally by means of micro particle image velocimetry (μPIV). Using this laser based technique, we are able to characterize quantitatively the velocity field at a given plane in the hyperbolic contraction region. The pressure drop across the converging geometry was also measured and was found to vary approximately linearly with the flow rate. Additionally, an extensive range of numerical calculations was carried out using a finite-volume method. The experimental results of velocity fields in the contraction and associated pressure drops compare very well with those predicted numerically. For the typical dimensions used in microfluidics, the flow is shown to be three-dimensional. Furthermore, we demonstrate that regions with nearly constant strain rate can only be achieved using geometries with large total Hencky strains under Hele-Shaw (potential-like) flow conditions.

1 Introduction

Extensionally-dominated flows are especially important in many applications involving non-Newtonian fluids, ranging from polymer processing (e.g. injection molding, spinning, film blowing) to inkjet printing or fertilizer spraying (Barnes et al. 1989). Optimization of these processes requires accurate measurements of the extensional properties of the fluid being processed. One of the most promising techniques applied for measurement of extensional viscosity involves studying the fluid flow through contractions profiled to give uniform extension rate (hyperbolic contractions) (Cogswell 1978). In this method, the pressure drop along the channel is measured to evaluate the resistance to fluid motion, which can be related to an apparent extensional viscosity. To remove the effect of shear at the walls of contractions Shaw (1975) proposed the use of a lubricating layer of low viscosity fluid that is injected at the walls near the upstream entrance. Although this is feasible for viscous fluids such as polymer melts, and results in correct measurements as shown by Everage and Ballman (1978), it is not an option when the fluids of interest are themselves low viscosity materials (such as inks or dyes or coating fluids).

James (1991) used a similarity transformation to analyze the steady flow of a viscous Newtonian fluid in an axisymmetric converging geometry with hyperbolic profile R^2z = constant (where R is the radius of the channel at the axial position z) so that the average velocity increases approximately linearly along the centerline. His analysis showed that at finite Reynolds numbers there is a homogeneous extensional flow within the central part of the contraction while the effects of shear are confined to a narrow boundary layer close to the wall. As the Reynolds number is increased further, viscous effects become less and less important, and the flow approaches a uniform potential flow in the inviscid limit. Experimental measurements and finite element calculations of the flow geometry showed good agreement with this similarity solution (James et al. 1990). Feigl et al. (2003) used the same type of converging geometry and showed that it is possible to obtain shear-free flow in which the extensional rate does not vary significantly along the core of the hyperbolic die under conditions of full slip at the walls. Although it is possible to promote wall-slip in polymer melts, it is hard to achieve complete slip in a controllable fashion, especially for low viscosity materials. In the present work, we thus wish to understand both experimentally and numerically the effects of viscous shear that is induced near the walls of planar hyperbolic contractions.

The measurement of extensional viscosity is still a challenging task, especially when dealing with dilute polymeric solutions. Inertial effects frequently dominate the elongational stresses at high

deformation rates (Hermansky and Boger 1995). The rapid development of soft lithography over the past decade has made possible the production of microfluidic devices with precise dimensions and at low-cost. Because of the small length-scales that characterize these flows (typically 100 μm or less), high deformation rates, yet small Reynolds numbers, are attainable in microfluidic flows. As a result, strong viscoelastic effects can be achieved in fluids that would otherwise behave essentially as Newtonian fluids in the equivalent macroscale flows (Groisman and Quake 2004, Rodd et al. 2005). This makes microfluidics an excellent technology platform for the development of an extensional rheometer for dilute polymer solutions. Rodd et al. (2005) studied the flow of dilute and semi-dilute polymer solutions through microgeometries consisting of an abrupt contraction followed by an abrupt expansion. More recently, Rodd et al. (2006) studied in detail the interplay of fluid inertia and fluid elasticity in this microgeometry and mapped the flow transition in a Weissenberg-Reynolds map using streakline photography, μPIV measurements and pressure drop measurements. Kang et al. (2005, 2006) have recently studied the pressure-driven flow of aqueous polymer solutions through microfabricated contractions and were able to achieve shear rates up to 10^6 s^{-1}. Measurements of the pressure drop through the contractions demonstrate that there can be substantial extra pressure losses associated with the extensional flow that arises when exiting, but mainly when entering the contraction region. Two types of end angle configurations were examined, 36° and 180° (abrupt contraction), and it was found that the end angle plays a negligible effect on the extra pressure drop and on polymer degradation. Tsai et al. (2006) have also examined numerically the flow of Newtonian fluids through microfabricated planar expansions, and demonstrated that the flow is locally three-dimensional near the expansion regime. Indeed, even for a slowly varying planar geometry the velocity field is highly three-dimensional as demonstrated analytically by Lauga et al. (2004), so the extension of this effect must be taken into account when devising rheometrical flows especially if they contain abrupt changes in cross-section. In designing and optimizing a microfluidic geometry it is thus essential to combine experimental measurements with high spatial and temporal resolution with numerical computations of the corresponding flow field.

This paper is part of ongoing work to characterize the extensional flow kinematics across converging micro-geometries and develop a device suitable for being used as an extensional rheometer. Here, we focus on steady Newtonian flow, as a preliminary study of the suitability of planar hyperbolic contraction geometries for maintaining a constant extensional rate through the converging region, an essential requirement to perform meaningful rheological measurements.

2 Experimental

2.1 Channel Geometry and Fabrication

The micro-geometries used in this work were planar and were designed to have a hyperbolic contraction section, in theory to provide a uniform strain rate deformation, followed by an abrupt expansion. Figure 1 shows a scanning electron microscopy (SEM) image and a transmission microscopy image of typical contraction–expansion geometries used. The channel depth, h, and the width of the upstream and downstream channels, $w_u = w_d$, were kept constant for all geometries used: $h = 46\ (\pm 1)$ μm and $w_u = w_d = 400$ μm, respectively. The total Hencky strain, defined as $\varepsilon_H = \ln\left(w_u / w_c\right)$ was varied from 1 to ln(40) which correspond to minimum contraction widths, w_c, at the expansion plane and contraction lengths, L_c, specified in Table 1. The Cartesian coordinate system is centered on the centerline, at the entrance plane of the contraction (cf. Figure 1b). For $0 \le z \le L_c$, the contraction wall is shaped according to following function $x = C/(a+z)$, where $a = L_c w_c/(w_u - w_c) = 20\,\mu\text{m}$ and $C = L_c w_u w_c/[2\ (w_u - w_c)] = 4000\ \mu\text{m}^2$.

Table 1 NEAR HERE

The channels were fabricated in polydimethylsiloxane (PDMS) from an SU-8 photoresist mold using standard soft-lithography techniques (McDonald et al. 2000; Ng et al. 2002). A high-resolution chrome mask together with a contrast enhancer and a barrier coat were employed to attain nearly vertical side-walls (with wall angles $87^\circ < \alpha < 92^\circ$) and well-defined corner features. A detailed description of the protocols for channel fabrication can be found in Scott (2004) and Rodd et al. (2005). Pressure taps were located 3 mm upstream and downstream of the contraction plane located at $z = 0$. A constant displacement-rate syringe pump (Harvard Apparatus PHD22/2000) was used to impose the flow rate into the micro-device over a wide range of flow rates ($0.1 \le Q \le 10$ ml/h) and Reynolds numbers ($0.32 \le Re \le 32.1$).

Fig. 1 NEAR HERE

2.2 Experimental Methods and Procedures

The results presented here were obtained using deionized water as the working fluid. The viscosity of the fluid was 0.94 mPa·s and the density 0.998 g/cm^3, both measured at 22.5ºC, the average temperature at which the experiments were carried out.

The flow through the contraction region was characterized experimentally using micro particle image velocimetry (μPIV) together with measurements of the total pressure drop across the contraction region. The latter data were achieved using differential pressure sensors (Honeywell 26PC) connected via flexible tubing to two pressure taps located 3 mm upstream and downstream of the contraction region. A calibrated pressure sensor, with 5 psi maximum measurable differential pressure, was used to cover pressure drops in the experimental range.

Micro Particle Image Velocimetry was used to measure the velocity field in the contraction region. This technique follows the basic principles of PIV for measuring the local velocities from the average displacement of tracer particles in a correlation region over a known time (Wereley and Meinhart 2004). The time separation between two consecutive frames was set according to flow conditions and the region of contraction under focus. As tracer particles we used 0.5μm diameter fluorescent particles (Ex/Em = 520/580 nm), which were added to the fluid at a mass concentration of 0.02%. A double-pulsed 532 nm Solo Nd:YAG laser system (15 mJ/pulse; New Wave Research), which was set to work at a pulse separation as short as 5 ns, was used for complete volume-illumination of the flow. A digital cross-correlation camera (1.4 MP PCO Sensicam; 1376 × 1024 pixels) connected to a Nikon microscope with a 20X objective lens (NA = 0.5) was used to acquire the images at a specific z-x planes. The depth of measurement (δz_m), i.e. the depth over which particle information contributes to the μPIV measurement, can be calculated as (Meinhart and Wereley 2000):

$$\delta z_m = \frac{3n\lambda_0}{NA^2} + \frac{2.16 d_p}{\tan\theta} + d_p \qquad (1)$$

provided that $d_p > e/M$, where NA is the numerical aperture of the objective, M the magnification, n the refractive index of the medium, λ_0 the wavelength of imaged light (in vacuum), $\theta = \sin^{-1}(NA/n)$, d_p the particle diameter and e the minimum resolvable feature size. For our specific optical set-up, e/M = 0.32 μm is smaller than the diameter of the tracer particles (0.5 μm) and the depth of measurement can be evaluated using equation (1). The calculated depth of measurement was 11.7 μm, which amounts to 25% of the channel depth. For each experiment, a minimum of 70 image pairs were

recorded, processed and ensemble averaged using Insight 6.0 software package from TSI. Each image was cross-correlated in interrogation areas of 32 × 32 pixels using a Nyquist algorithm with a 50% overlap to generate two-dimensional velocity vector maps.

3 Numerical

3.1 Governing Equations and numerical method

For an incompressible fluid flow, the governing equations for conservation of mass and momentum can be expressed as follows:

$$\nabla \cdot \mathbf{u} = 0 \tag{2}$$

$$\rho\left[\frac{\partial \mathbf{u}}{\partial t} + \nabla \cdot \mathbf{u}\mathbf{u}\right] = -\nabla p + \nabla \cdot \boldsymbol{\tau}_T \tag{3}$$

where ρ is the density of the fluid, t the time, $\mathbf{u}$ the velocity vector, p the pressure and $\boldsymbol{\tau}_T$ the total extra stress tensor. In the case of a Newtonian fluid, the total extra stress tensor becomes $\boldsymbol{\tau}_T = \boldsymbol{\tau}_S = \eta_S\left(\nabla\mathbf{u} + \nabla\mathbf{u}^{\mathrm{T}}\right)$, where η_S is the solvent viscosity. The numerical code used here is applicable to a broad range of viscoelastic models, and therefore the constitutive equation, even for the simple case of a Newtonian flow, is solved separately from the momentum equation (Oliveira et al. 1998, Oliveira and Pinho 1999, Oliveira et al. 2006).

Equations (2) and (3) assume the validity of the continuum hypothesis, which has been questioned in a number of works related to microfluidic applications (Pit et al. 2000; Barrat and Bocquet 1999). However, for liquid flows at these micrometer length scales it has been well established that the basic laws expressed by equations (2) – (3) and the no-slip boundary condition at the walls remain valid (Whitesides and Stroock 2001, Karniadakis et al. 2005). The agreement between experimental results and the numerical simulations here presented will further give credit to this assumption, at least for Newtonian fluids and the material used here to fabricate the microgeometries.

The governing equations above are solved numerically using a finite volume method with a time marching algorithm (Oliveira et al. 1998). In this methodology, the resulting algebraic equations relate the dependent variables (p, $\mathbf{u}$, $\boldsymbol{\tau}$), which are calculated at the center of the cells forming the computational mesh, to the values in the nearby surrounding cells. Non-orthogonal non-uniform block-

structured meshes are used to map the computational domain. Central differences are used to discretize the diffusive terms, while the CUBISTA high-resolution scheme (Alves et al. 2003) is employed in the discretization of the advective terms. Because we are interested in steady-state calculations in the present work, the time derivative is discretized with an implicit first-order Euler scheme.

No-slip conditions at the solid walls were imposed as well as symmetry conditions at the two center planes ($x = 0$ and $y = 0$). Therefore, the governing equations were solved in only a quarter of the complete flow domain as explained in the next section (cf. Figure 2). The outflow boundary condition imposed involves vanishing streamwise gradients ($\partial / \partial x = 0$) of velocity and stress components and a constant gradient of pressure at the downstream channel outlet ($L = L_d$). At the inlet boundary, located well upstream of the region of interest, a uniform velocity profile and null stress components were imposed.

3.2 Computational domain, meshes and dimensionless numbers

Figure 2 gives a zoom view of a typical mesh used in the computations near the contraction region. The inlet and outlet lengths of the channel were set to be longer ($L_u = L_d = 30 w_u$) than in the actual experimental device to ensure that the flow fully develops upstream of the contraction and completely re-develops downstream of the expansion.

Fig. 2 NEAR HERE

The computational meshes were composed of 5 structured blocks and the total number of cells varied depending on the Hencky strain used, which is closely related to the definition of contraction ratio, $CR = \exp(\varepsilon_H)$. Another important geometric parameter considered is the aspect ratio defined as $AR = w/h$. Table 2 shows some of the mesh characteristics, such as the number of cells (NC) and the minimum cell size, of the main four meshes used. These correspond to the experimental geometries described in section 2.1 ($h = 46$ μm).

Table 2 NEAR HERE

The other relevant dimensionless variable that characterizes the dynamics of the flow through the microgeometry is the Reynolds (*Re*) number, here defined as:

$$Re = \frac{\rho < V_z >_u w_u / 2}{\eta_S} = \frac{\rho Q}{2h\eta_S} \tag{4}$$

where Q is the volumetric flow rate and $< V_z >_u$ is the average velocity in the upstream channel ($< V_z >_u = Q / h\, w_u$). For the present conditions and geometries, using water as working fluid, Re = 3.21 Q, with Q expressed in ml/h.

4 Results

The kinematics of the flow in the planar geometry was quantified using μPIV as described in section 2.2. The first step towards the validation process of the experimental measurements comprised a comparison of the axial velocity profiles obtained experimentally in the large upstream rectangular duct, where the flow is fully developed (i.e. well upstream of the contraction plane), to the corresponding analytical solution for a Newtonian fluid given by (White 1991):

$$V_z(x,y) = \frac{12Q}{ab\pi^3} \frac{\sum_{i=1,3,\ldots}^{\infty} \frac{(-1)^{(i-1)/2}}{i^3} \cos(i\pi x/2a)\left(1 - \frac{\cosh(i\pi y/2a)}{\cosh(i\pi b/2a)}\right)}{\left(1 - \frac{192a}{\pi^5 b} \sum_{1=1,3,\ldots}^{\infty} \frac{\tanh(i\pi b/2a)}{i^5}\right)} \tag{5}$$

where V_z is the axial velocity, a is the upstream half-width (w_u/2) and b is the channel half-depth (h/2).

In Figure 3a, we show the axial velocity profile along the lateral direction at the center plane (y = 0). This profile was obtained from a single experiment in the standard way, i.e. using a single set of 70 images pairs centered at the y = 0 plane from which the velocity profile along direction x is obtained. In Figure 3b, the axial velocity profile along the out-of-plane direction at x = 0 plane is shown. In this case, each point was obtained from a different "illumination" experiment at a different y-plane. For each out-of-plane position, the velocity field was measured as described above, and the velocity plateau of the lateral profiles was determined and taken to represent the velocity on the y-z center plane at x = 0 for that particular value of y. This procedure was repeated for various positions through the whole depth of the channel to construct Figure 3b. A close agreement is found between the experimental measurements and the analytical solutions thus validating the experimental procedure.

Fig. 3 NEAR HERE

The transverse velocity profiles along the center plane ($y = 0$) are illustrated in Figure 4 for $Q = 1$ ml/h ($Re = 3.21$) through the geometry with a total Hencky strain of two $(\varepsilon_H = 2)$. The plot includes both experimentally measured and numerically calculated velocity profiles for various axial positions (-400 μm $\leq z \leq$ 80 μm). In Figure 4a, we depict the axial velocity component V_z and in Figure 4b the lateral velocity component V_x. For an axial position far upstream of the contraction plane (z = -400 μm), the profiles resemble those of fully-developed flow. As we move towards the contraction plane, the fluid is drawn towards the centerline. This causes the axial velocity near the walls to decrease, while the lateral velocity increases substantially relative to the fully developed flow. The maximum velocity attained at the centerline ($y = 0$, $x = 0$) increases as we progress along the contraction. Excellent agreement of the numerical predictions with the experimental data is found in the whole flow region.

Fig. 4 NEAR HERE

The measured and numerically predicted axial velocities along the centerline are also compared in Figure 5. Figure 5a shows the effect of the flow rate for a fixed Hencky strain ($\varepsilon_H = 2$) and Figure 5b illustrates the effect of the total Hencky strain at a fixed Reynolds number ($Re = 3.21$; $Q = 1$ ml/h).

Fig. 5 NEAR HERE

The profiles evolve from fully developed in the far upstream part of the channel (where the centerline velocity is constant) to a region where the fluid accelerates as the contraction plane is approached. Within the hyperbolic contraction the axial velocity increases considerably as the channel gets narrower. As the fluid crosses the expansion, it decelerates until the flow re-develops downstream of the contraction. The channel length required for the fluid to regain its fully developed condition depends on the flow rate (Reynolds number) as in macroscale flows. To make this clear, we present the dimensionless axial velocity scaled with the average upstream velocity, $\langle V_z \rangle_u$, in the inset of Figure 5a, where only the numerical results are displayed, for clarity.

For the higher Hencky strain geometries (e.g. $\varepsilon_H = 3$), there is also a region of the converging die, very close to the expansion plane, where the velocity shows an upward kink (highlighted by the dotted ellipse in Figure 5b). This is the region where the axial velocity reaches its maximum value and it extends from z = 370 μm up to z = 377 μm. Experimentally, this upward kink is hard to identify in Figure 5b for the experiments done at $\varepsilon_H = 3$, due to limitations in the experimental technique. The

quality of the images, which are crucial to obtaining precise results, are adversely affected by glowing of the walls and/or by the accumulation of particles near the end of the contraction. For high strains, where the width of the channel in this region is very small, these undesired effects are magnified and as a consequence the quality of the PIV results deteriorates.

Fig. 6 NEAR HERE

By a detailed inspection of the predicted streaklines, it is clear that this feature is related to three-dimensional effects. Although this effect is barely noticeable at a total Hencky strain of 3, numerical results show that it is enhanced for higher Hencky strains, e.g. $\varepsilon_H = \ln(40)$ (c.f. top curve in the inset of Figure 5b). Figure 6 shows the numerically predicted streaklines close to the expansion region at the center plane ($y = 0$, Figure 6a) and at plane $x = 0$ (Figure 6b), for the geometry with a total Hencky strain $\varepsilon_H = 3$ at a flow rate $Q = 1$ ml/h. In the region of the die where to the kink in the axial velocity was observed, the out-of-plane streaklines move closer to the centerline ($x = y = 0$) as the fluid approaches the expansion plane (c.f. Figure 6b). It should also be noted that both for $\varepsilon_H = 3$ and ln(40), the fluid starts to decelerate before it even crosses the expansion plane, at an axial position of $z \approx 380$ μm for $\varepsilon_H = 3$ and $z \approx 760$ μm for $\varepsilon_H = \ln(40)$. This can be easily understood by inspection of the in-plane streaklines in Figure 6a that start to move away from the centerline due to the expansion.

It is clear from the experimental results that at the higher Hencky strains the velocity profiles become harder to measure near the expansion plane, because of the proximity of the walls, the larger velocity gradients and the high contraction ratios. Nevertheless, the experimental results are in good agreement with the numerical solutions for all cases studied, as can be assessed from the axial velocity contour plots at the center plane ($y = 0$) in Figure 7. The experimental contour plots were constructed from the original velocity vector maps, which are shown in Figure 8 for two different Hencky strains and flow rates. Although the experimental contour plots are not as smooth as the corresponding numerical plots, the μPIV and computed velocity fields are in good agreement. In Figure 7, we also compare the velocity fields at different Hencky strains for the same flow rate. It is interesting to note that, whereas the maximum axial velocity for the Hencky strain of two is located at the centerline, as observed previously in Figures 4, in the smaller Hencky strain case two off-center velocity maxima are observed both experimentally and numerically.

Fig. 7 NEAR HERE

Fig. 8 NEAR HERE

As already discussed, three-dimensional effects play an important role in this flow and similarly, the development of off-center maxima was seen to be closely related to the geometry depth and therefore to the aspect ratio. To investigate this issue, Figure 9 shows the effect of the out-of-plane channel depth h on the computed axial velocity profile along the lateral direction at the expansion plane. These results were obtained for creeping flow conditions ($Re = 0$) at the center plane for a contraction with $\varepsilon_H = 1$.

Fig. 9 NEAR HERE

As anticipated from Figure 7, for the depth used in the experiments, $h = 46$ μm, the maximum velocity is already located off-center. The peak corresponding to the maximum velocity is seen to become more pronounced and moves towards the reentrant expansion corner as the channel depth decreases. At the smaller depths used in the calculations, the diffusive fluxes of momentum in the y-direction "dominate" compared to those in other directions and changes in geometry in x-z planes act slowly. Therefore the flow at constant y-planes approaches a 2D potential flow, as illustrated in Fig. 9 for the center plane ($y = 0$). In Figure 10a, we compare the axial velocity contour plot at the center plane for $h = 46$ μm with that for smaller ($h = 4.6$ μm) and larger ($h = 460$ μm) depths. Increasing the depth of the channel makes diffusion in the x-z plane dominate over diffusion in the y-direction and the flow in the center plane approaches a 2D Stokes flow (e.g. $h = 460$ μm). In this case, there is only one maximum located at the centerline ($x = 0$).

To show that this is not a particularity of the geometry corresponding to $\varepsilon_H = 1$, we have extended this analysis to the four Hencky strains used. Figure 10b shows the corresponding contour plots for $\varepsilon_H = 3$ and $h = 0.46$, 4.6, 46 μm. Again, we observe that as h decreases, the maximum axial velocity approaches the expansion corners, as expected for a Hele-Shaw flow. However, the observation of off-center maxima requires now a smaller value of h since the width of the channel at the expansion is less than for $\varepsilon_H = 1$, i.e., this phenomenon is indirectly controlled by the ratio h/w.

Fig. 10 NEAR HERE

A series of numerically predicted streaklines are shown in Figure 11 for $\varepsilon_H = 2$ and increasing flow rates. An increase in flow rate, and therefore in the Reynolds number, results in the development and enhancement of a lip vortex downstream of the expansion plane (e.g. *Re* = 16.0, *Q* = 5 ml/h). The recirculation grows with inertia and at *Re* = 25.6 (*Q* = 8 ml/h) it already extends to the side wall close to the salient corner ($x = \pm 200$ μm). The vortices continue to expand downstream for the entire range of flow rates tested (up to *Re* = 32.1; *Q* = 10 ml/h). Eventually, a flow asymmetry will develop at higher flow rates, as usually observed in 2D-planar expansion flows (Wille and Fernholz 1965, Chiang et al. 2000, Oliveira 2003). However the imposition of symmetry at planes $x = 0$ and $y = 0$ inhibits the occurrence of this expected bifurcation. For that reason, we have refrained from increasing the flow rates even further in the simulations.

Fig. 11 NEAR HERE

For the sake of comparison, in Figure 12 we overlap the predicted streaklines upstream and in the contraction region at a "low" and at a "high" flow rate, *Q* = 1 ml/h (*Re* = 3.21) and *Q* = 10 ml/h (*Re* = 32.1), respectively. As we move closer to the contraction plane, the fluid is forced towards the centerline and the streaklines are similar for the two flow rates, but two main differences should be noted: i) at the contraction region, the streaklines corresponding to the higher flow rate are pushed closer to the wall due to the higher streamwise velocities (and the increased importance of fluid inertia); ii) at the expansion plane, fluid elements at the lower flow rate begin to reattach to the wall as soon as they exit the contraction, while inertial effects keep the corresponding streaklines at higher flow rate moving straight for a longer distance resulting in the formation of a large recirculation.

Fig. 12 NEAR HERE

The vortex size depends not only on the Reynolds number but also on the expansion ratio as shown in Figure 13, where the predicted streaklines are depicted for a fixed flow rate and four different Hencky strains. The streaklines of Figure 13 show the effect of Hencky strain at a constant non-negligible Reynolds number of 9.62. At low Hencky strains the behaviour is akin to that of creeping flow in the sense that there is no flow separation, but as the gap at the end of the contraction narrows and the exit jet strengthens the lip vortex forms and expands. Overall, the vortex enhancement mechanism is similar to that observed in studies of planar geometries with abrupt contraction-expansion (Rodd et al. 2005, Townsend and Walters 1994).

Fig. 13 NEAR HERE

The strain rates for each set of flow conditions can be computed from the axial velocity profiles along the hyperbolic contraction region. Figure 14 shows the velocity profiles and the strain rate profiles along the centerline for the flow conditions corresponding to Figure 5a. We compare the numerical (thick solid lines) and experimental (symbols) results with the values calculated using the theoretical axial velocity at the centerline (assuming that at each axial location the flow fully develops instantaneously), which is related to the average velocity by (White 1991):

$$V_{z,\,centerline} = k < V_z > \tag{6}$$

Assuming that the Newtonian fluid flow along the contraction is locally fully developed these values of k are only a function of the channel aspect ratio and are obtained from the exact fully-developed solution in a rectangular channel (Equation 5). These analytical results are shown as thin solid lines in Figure 14. The differences between these analytical results and the actual numerical (and experimental) data are mainly a consequence of not considering contraction entrance and expansion exit effects.

Fig. 14 NEAR HERE

It can be clearly observed in Figure 14b that the strain rate is not constant along the contraction. In addition to entrance and exit effects, which spread to most of the contraction length, there are two other effects that should be taken into consideration. Firstly, the aspect ratio (h/w) is not constant along the contraction and therefore the strain rate also varies, even for the hypothetical fully developed case. Finally, we should also point out that this is a viscous flow and wall effects are not negligible.

For the sake of comparison, we have also plotted, as dashed lines in Figure 14, the results obtained if the velocity varied linearly from the entrance to the exit of the contraction. In this ideal case, the strain rate at the centerline is assumed constant and can be calculated as:

$$\dot{\varepsilon}_{centerline} = \left(k_c \frac{Q}{h\,w_c} - k_u \frac{Q}{h\,w_u} \right) \Big/ L_c \tag{7}$$

where k_u and k_c were determined from Equations 5 and 6. For the geometry with $\varepsilon_H = 2$, the parameters k_u and k_c are approximately 1.62 and 2.09 at the contraction entrance (AR = 8.7) and exit (AR = 1.2), respectively.

For a converging geometry with a higher Hencky strain, it is expected that there will be a region of the contraction which is not affected by entrance and/or exit effects. However, the strain rate is only truly constant as 2D-potential flow is approached, i.e. when either the Reynolds number is high or when the depth of the channel is substantially smaller than the channel width leading to a Hele-Shaw flow. This asymptotic behavior is demonstrated in Figure 15 where it is also interesting to note that entrance effects are approximately the same independently of the geometry (Hencky strain) used, particularly when h is small (i.e. when a Hele-Shaw flow is approached). As the depth is reduced, the flow streaklines become independent of y (even though the velocity components exhibit a strong dependence) and coincident with those observed for an inviscid fluid. Therefore, a significant region of constant strain rate is observed. Although reducing h may seem like an appropriate way to achieve a homogeneous extensional flow, it leads to strong shear effects due to the increase in τ_{zy} (and in pressure drop) and the dimensionless excess entry pressure drop due to extensional effects decreases substantially (Oliveira et al. 2006), which makes it unfeasible to extract an apparent extensional viscosity simply from pressure drop measurements.

Fig. 15 NEAR HERE

The pressure drop across the hyperbolic contraction was also measured experimentally. In Figure 16, we compare the experimental global pressure drop ΔP between the two pressure taps (located 3 mm upstream and downstream of the contraction plane) to the corresponding numerical estimate for the Newtonian fluid. We examine the effect of Reynolds number by varying the flow rate in the range 0.4 ml/h < Q < 10 ml/h (1.28 < Re < 32.1). There is a clear trend of the pressure drop to increase with flow rate. For the range of flow rates covered, the pressure drop is seen to increase almost linearly with the flow rate and a close agreement is observed between the numerical and experimental results. For comparison, we have also plotted the hypothetical pressure drop determined assuming that the flow fully-develops instantaneously at each axial position. This estimate is expected to be accurate whenever the channel cross-section varies smoothly along the axial position (Lauga et al 2004). In the micro geometries used in this work there are sudden changes of the cross-section on the entrance and exit of the hyperbolic section, therefore it is not surprising that this estimate of the hypothetical

pressure drop assuming fully-developed profiles is consistently lower than the corresponding measured values.

Fig. 16 NEAR HERE

5 Conclusions

We have presented a detailed study on the flow of a Newtonian fluid through 3D-planar micro-geometries containing a hyperbolic contraction followed by an abrupt expansion. The work was carried out from both an experimental and a numerical perspective and the corresponding results are in good agreement with each other. Although at first sight the flow may resemble quasi-two dimensional in nature, it has been shown here that there are important three-dimensional effects, which depend on the aspect ratio and a simple 2-D is often qualitatively inadequate to describe the flow patterns. Interestingly, for geometries with high aspect ratios a Hele-Shaw flow approximation is legitimate and therefore the flow patterns resemble those of 2D-potential flow, and not planar two-dimensional viscous flow as usually assumed erroneously in numerical works in microfluidics.

The experimental laser-based μPIV technique allows for accurate measurements of the velocity field in the contraction region for a range of flow rates (1ml/h $\leq Q \leq$ 3ml/h) and Hencky strains ($1 \leq \varepsilon_H \leq 3$). In the upstream channel away from the contraction the axial velocity profiles resemble those of fully developed flow, but as the fluid approches the contraction, it is drawn towards the centerline and the maximum centerline velocity increases. As the Reynolds number is increased expansion effects are felt further downstream and lip vortices are seen to develop and grow downstream of the contraction. The development of single centered velocity maximum or double off-center velocity maxima at the contraction neck have also been measured and accurately predicted numerically. Experimental measurements of pressure drop were also performed and could be extended to a wider range of flow conditions than those reached using μPIV. The pressure drop across the contraction was found to vary approximately linearly with the Reynolds number, but contrary to our expectations, the strain rate along the centerline of the converging geometry with a Hencky strain of two was not constant. For this geometry, the length of the contraction was not sufficient to guarantee the existence of a region without important entrance and exit effects. Furthermore, the wall effects are not negligible and the aspect ratio varies along the contraction. For the higher strains, this is not as severe and there is a region of approximately linear velocity as the geometry depth is reduced. Even so, the problem is still

far from being overcome and a serious effort to optimize the shape of the converging geometry is essential if this type of configuration is to be used (within the scope of microfluidics) as an extensional rheometer. The work presented here is a starting point for a more in-depth study of the flow of viscoelastic fluids in this type of micro-geometries. However, as we have demonstrated, even for a simple Newtonian fluid the flow in this type of micro-geometries is highly complex and is yet to be completely understood.

6 Acknowledgments

M. S. N. Oliveira would like to thank Fundação para a Ciência e a Tecnologia (FCT), Portugal for financial support (SFRH/BPD/15005/2004). M. S. N. Oliveira, M. A. Alves and F. T. Pinho acknowledge the financial support provided under program POCI2010 by FCT and FEDER: project POCI/EME/59338/2004 (M. S. N. Oliveira; M. A. Alves; and F. T. Pinho) and project POCI/EQU/59256/2004 (M. A. Alves). The experimental portion of this work was carried out in the Hatsopoulos Microfluids Laboratory at MIT using equipment provided by the National Science Foundation under grant CTS-0116486.

7 References

Alves MA, Oliveira PJ, Pinho FT (2003) A convergent and universally bounded interpolation scheme for the treatment of advection. Int J Numer Meth Fl 41: 47-75.

Barnes HA, Hutton JF, Walters K (1989) An introduction to rheology. Elsevier, Amsterdam.

Barrat JL, Bocquet L (1999) Large slip effect at a nonwetting fluid-solid interface. Phys Rev Lett 82: 4671-4674.

Chiang TP, Sheu TWH, Wang SK (2000) Side wall effects on the structure of laminar flow over a plane-symmetric sudden expansion. Comput Fluids 29: 467-492.

Cogswell FN (1978) Converging flow and stretching flow: a compilation. J Non-Newton Fluid 4: 23-38.

Everage Jr AE, Ballman RL (1978) The extensional flow capillary as a new method for extensional viscosity measurement. Nature 273: 213-215.

Feigl K, Tanner FX, Edwards BJ, Collier JR (2003) A numerical study of the measurement of elongational viscosity of polymeric fluids in semi-hyperbolically converging die. J Non-Newton Fluid 115: 191-215.

Groisman A, Quake SR (2004) A microfluidic rectifier: Anisotropic flow resistance at low Reynolds numbers. Phys Rev Lett 92: 1-4.

Hermansky CG, Boger DV (1995) Opposing-jet viscometry of fluids with viscosity approaching that of water. J Non-Newton Fluid 56: 1-14.

James DF (1991) Flow in a converging channel at moderate Reynolds number. AIChE J 37: 59-64.

James DF, Chandler GM, Armour SJ (1990) A converging channel rheometer for the measurement of extensional viscosity. J Non-Newton Fluid 35: 421-443.

Karniadakis G, Beskok A, Aluru NR (2005) Microflows and nanoflows: fundamentals and simulation. New York, NY, Springer Verlag.

Kang K, Koelling KW, Lee LJ (2006) Microdevice end pressure evaluations with Bagley correction. Microfluid Nanofluid 2:223-235.

Kang K, Lee LJ, Koelling KW (2005) High shear microfluidics and its application in rheological measurement. Exp Fluids 38: 222-232.

Lauga E, Stroock AD, Stone HA (2004) Three-dimensional flows in slowly varying planar geometries. Phys Fluid 16: 3051-3062.

McDonald JC, Duffy DC, Anderson JR, Chiu DT, Wu HK, Schueller OJA, Whitesides GM (2000) Fabrication of microfluidic systems in poly(dimethylsiloxane). Electrophoresis 21: 27-40.

Meinhart CD, Wereley ST, Gray MHB (2000) Volume illumination for two-dimensional particle image velocimetry. Meas Sci Technol 11: 809-814.

Ng JMK, Gitlin I, Stroock AD, Whitesides GM (2002) Components for integrated poly(dimethylsiloxane) microfluidic systems. Electrophoresis 23: 3461-3473.

Oliveira MSN, Rodd LE, McKinley GH, Alves MA (2006) Simulations of extensional flow in microrheometric devices. *To be submitted to* Microfluid and Nanofluid.

Oliveira PJ (2003) Asymmetric flows of viscoelastic fluids in symmetric planar expansion geometries. J Non-Newton Fluid 114: 33-63.

Oliveira PJ, Pinho FT (1999) Numerical procedure for the computation of fluid flow with arbitrary stress-strain relationships. Numer Heat Tr B-Fund 35: 295-315.

Oliveira PJ, Pinho FT, Pinto GA (1998) Numerical simulation of non-linear elastic flows with a general collocated finite-volume method. J Non-Newton Fluid 79: 1-43.

Pit R, Hervet H, Leger L (2000) Direct experimental evidence of slip in hexadecane: Solid interfaces. Phys Rev Lett 85: 980-983.

Rodd LE, Cooper-White JJ, Boger DV, McKinley GH (2005) Role of the elasticity number in the entry flow of dilute polymer solutions in micro-fabricated contraction geometries. J Non-Newton Fluid 129: 1-22.

Rodd LE, Scott TP, Boger DV, Cooper-White JJ, McKinley GH (2006) The inertio-elastic planar entry flow of low-viscosity elastic fluids in micro-fabricated geometries. *Submitted to* J Non-Newton Fluid.

Scott TP (2004) Contraction/expansion flow of dilute elastic solutions in microchannels. Master thesis, Mechanical Engineering Department. MIT, Cambridge, MA, USA.

Shaw MT (1975) Flow of Polymer Melts through a Well-Lubricated, Conical Die. J Appl Polym Sci 19: 2811-2816.

Tsai C-H, Chen H-T, Wang Y-N, Lin C-H, Fu L-M (2006) Capabilities and limitations of 2-dimensional and 3-dimensional numerical methods in modeling the fluid flow in sudden expansion microchannels. Microfluid and Nanofluid DOI 10.1007/s10404-006-0099-2.

Townsend P, Walters K (1994) Expansion flows of non-newtonian liquids. Chem Eng Sci 49: 749–763.

Wereley ST, Meinhart CD (2004) Micron-Resolution Particle Image Velocimetry. In: Microscale Diagnostic Techniques (Breuer KS, ed.). Berlin, Heidelberg, New York: Springer.

White FM (1991) Viscous fluid flow. New York, McGraw-Hill.

Whitesides GM, Stroock AD (2001) Flexible methods for microfluidics. Phys Today 54: 42-48.

Wille R, Fernholz H (1965) Report on First European Mechanics Colloquium on Coanda Effect. J Fluid Mech 23: 801-819.

LIST OF FIGURES

Fig. 1 Experimental micro-geometry with a hyperbolic contraction: (a) SEM image ($\varepsilon_H = 2$); (b) Optical transmission microscope image ($\varepsilon_H = 3$).

Fig. 2 Zoomed view of the mesh M2 and detail near the expansion plane.

Fig. 3 Comparison of the axial velocity profiles determined experimentally (closed symbols) at constant flow rate Q = 1ml/h (Re = 3.21) and the analytical solution (solid lines) for Newtonian flow in a rectangular channel (400×46 μm^2): (a) Profile along the x-axis direction (y = 0); (b) Profile along the y-axis direction (x = 0).

Fig. 4 Comparison of the velocity profiles at the center plane (y = 0) determined experimentally (open symbols) and numerically (solid lines), as a function of the axial and lateral positions for Q = 1 ml/h (Re = 3.21): (a) Velocity component in the z-axis direction; (b) Velocity component in the x-axis direction.

Fig. 5 Axial velocity profile along the centerline (y = 0, x = 0) measured experimentally (open symbols) and calculated numerically (solid lines). (a) Effect of flow rate at a fixed total Hencky strain, $\varepsilon_H = 2$; (b) Effect of the total Hencky strain at a fixed flow rate Q = 1 ml/h (Re = 3.21).The inset shows numerical results at Hencky strains of 1, 2, 3 and ln(40). The dashed vertical lines indicate the beginning and end of the contraction sections.

Fig. 6 Predicted streaklines for ε_H = 3 and Q = 1 ml/h (Re = 3.21): (a) at the center plane (y = 0); (b) at the z-y plane with x = 0. The vertical light lines mark the beginning and end of the contraction. Note that the axes are not to scale.

Fig. 7 Axial velocity contour plots at the center plane (y = 0) at Q = 1 ml/h (Re = 3.21). Comparison between experimental measurements (left) and numerical predictions (right) for: (a) $\varepsilon_H = 2$; (b) $\varepsilon_H = 1$.

Fig. 8 Experimental velocity vector maps at the center plane (y = 0): (a) Q = 3 ml/h (Re = 9.62) and ε_H = 2 (b) Q = 1 ml/h (Re = 3.21) and ε_H = 3. For clarity, only a quarter of the total number of vectors are shown.

Fig. 9 Axial velocity profiles predicted numerically under creeping flow conditions at the intersection between the center plane (y = 0) and the expansion plane (z = 34.4 μm) for $\varepsilon_H = 1$ and a range of depths $4 \le h \le 460$ μm.

Fig. 10 Numerical contour plots of the normalized axial velocity ($V_z / V_{z,max}$) at the center plane ($y = 0$) obtained under creeping flow conditions for (a) $\varepsilon_H = 1$ and (b) $\varepsilon_H = 3$.

Fig. 11 Numerically predicted streaklines at the center plane ($y = 0$) for $\varepsilon_H = 2$ and increasing flow rates.

Fig. 12 Predicted streaklines for $\varepsilon_H = 2$: Q = 1 ml/h, Re = 3.21 (thin lines); Q = 10 ml/h, Re = 32.1 (thick lines).

Fig. 13 Numerically predicted streaklines at the center plane ($y = 0$) for Re = 9.62 (Q = 3 ml/h) and four different Hencky strains.

Fig. 14 Velocity profiles (a) and strain rate profiles (b) along the centerline for $\varepsilon_H = 2$: Q = 1 ml/h, Re = 3.21 (□); Q = 2 ml/h, Re = 6.41 (△) and Q = 3 ml/h, Re = 9.62 (○). The symbols correspond to experimental data, the thick lines to data from numerical predictions, the thin lines to the hypothetical fully developed case (equation 6) and the dashed lines to the ideal case with a linear variation between the contraction entrance and exit (equation 7).

Fig. 15 Strain rate profiles along the centerline under creeping flow conditions for ε_H = 2 (dashed lines) and ε_H = 3 (solid lines).

Fig. 16 Effect of flow rate on the total pressure drop determined experimentally (open symbols) and numerically (closed symbols) for ε_H = 1 and 2. The solid lines correspond to hypothetical pressure drops if there were no entrance or exit effects and assuming the flow is fully-developed everywhere.

Table 1 Geometry characteristic dimensions

Hencky strain, ε_H	**L_c (μm)**	**w_c (μm)**
1	34.4	147
2	128	54.1
3	382	19.9
ln(40)	780	10.0

Table 2 Main characteristics of the computational meshes

Mesh	**Hencky Strain**	**NC**	$\Delta x_{\min} / w_c$	$\Delta y_{\min} / w_c$	$\Delta z_{\min} / w_c$
M1	1	49920	0.011	0.011	0.010
M2	2	50080	0.024	0.022	0.025
M3	3	66720	0.026	0.025	0.026
M4	ln(40)	84160	0.033	0.031	0.032

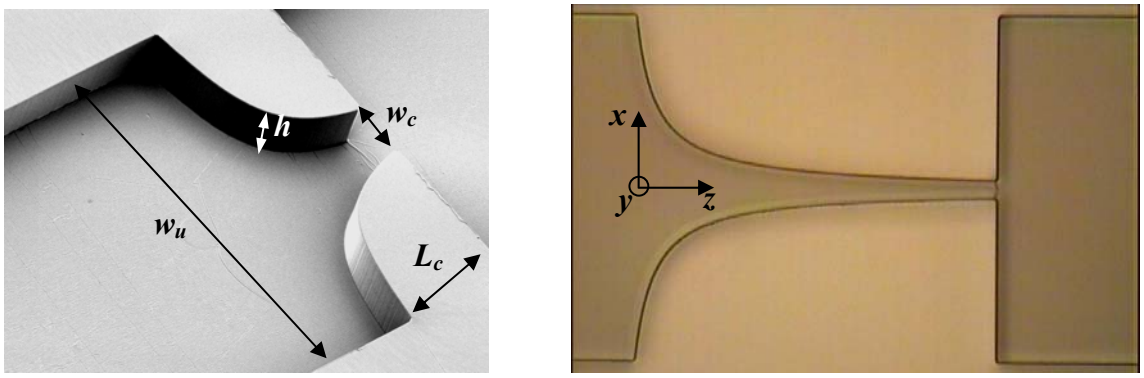

(a) (b)

Fig. 1 Experimental micro-geometry with a hyperbolic contraction:
(a) SEM image ($\varepsilon_H = 2$); (b) Optical transmission microscope image ($\varepsilon_H = 3$).

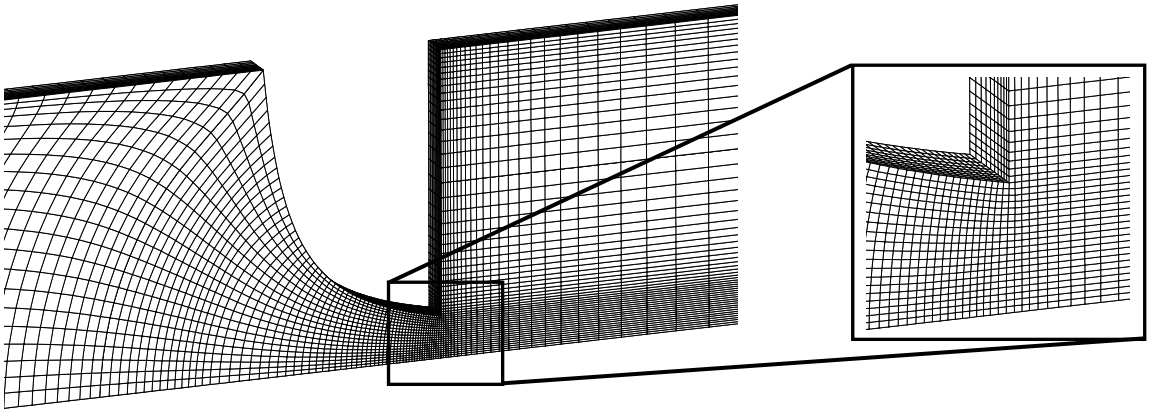

Fig. 2 Zoomed view of the mesh M2 and detail near the expansion plane ($\varepsilon_H = 2$).

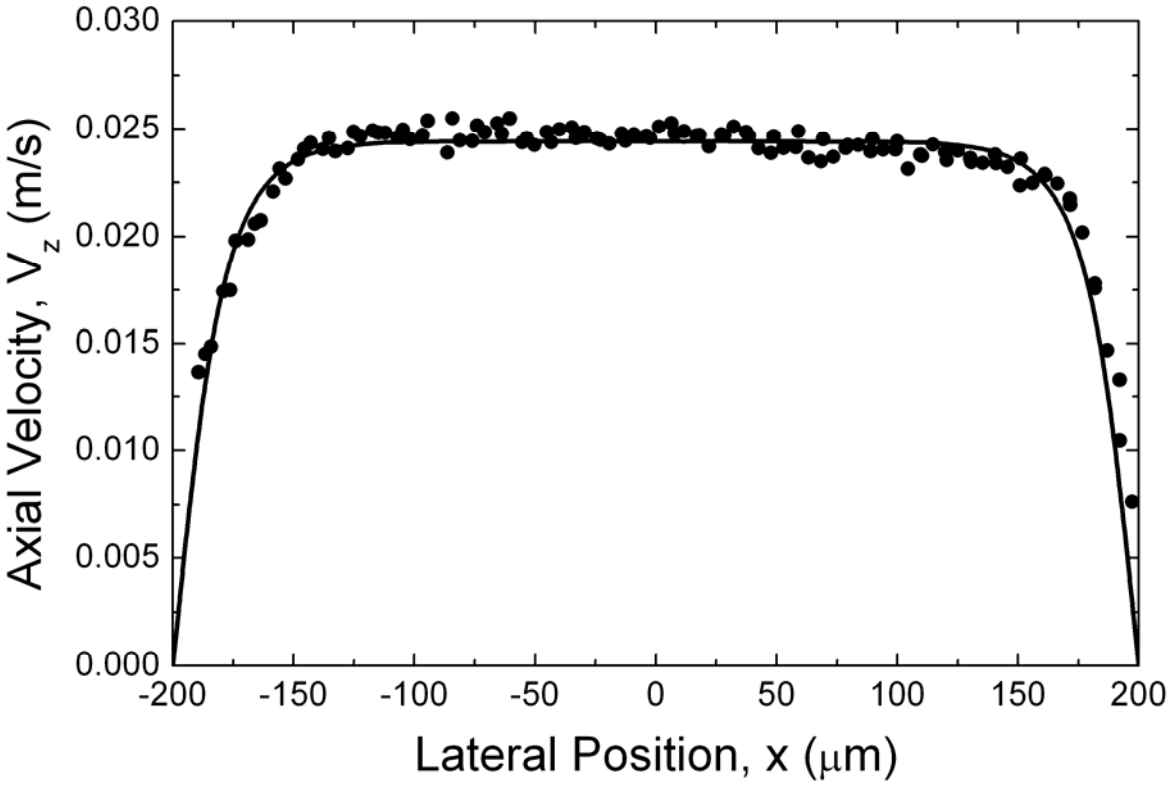

(a)

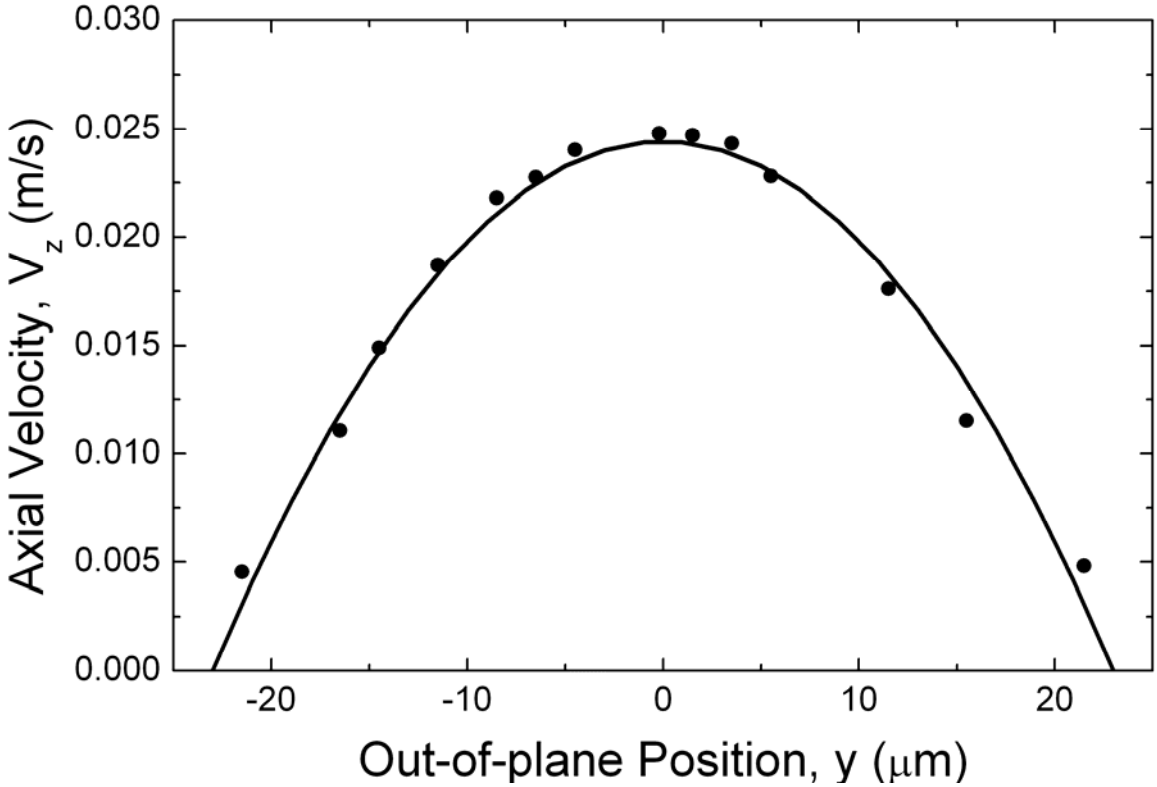

(b)

Fig. 3 Comparison of the axial velocity profiles determined experimentally (closed symbols) at constant flow rate Q = 1ml/h (Re = 3.21) and the analytical solution (solid lines) for Newtonian flow in a rectangular channel (400×46 μm^2): (a) Profile along the x-axis direction (y = 0); (b) Profile along the y-axis direction (x = 0).

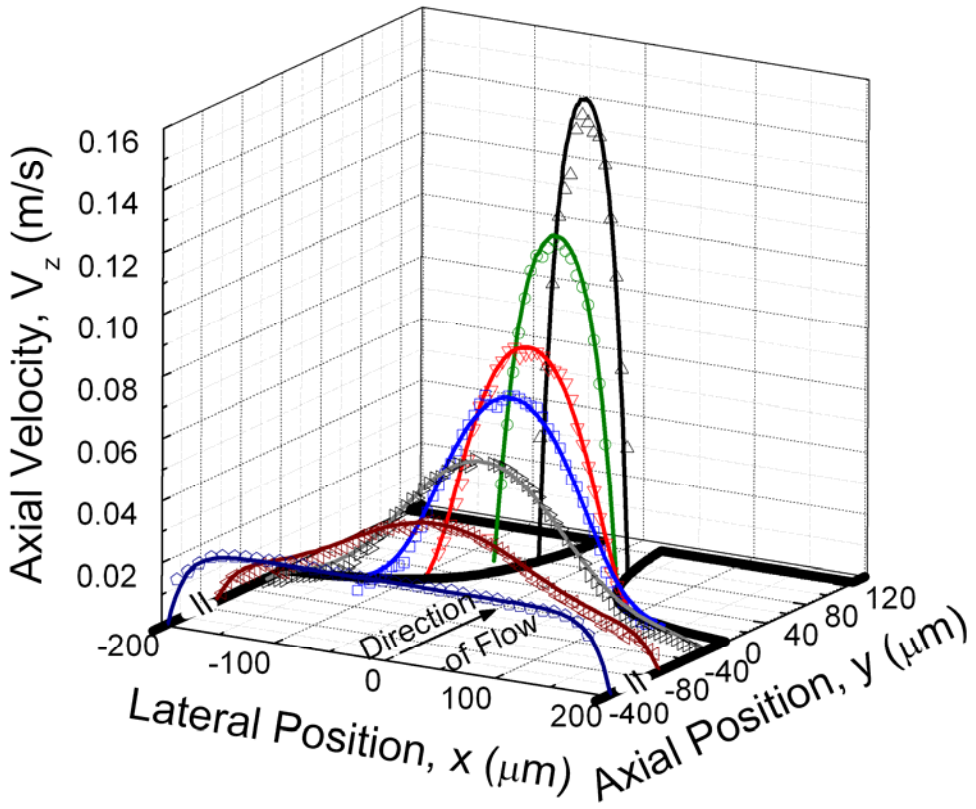

(a)

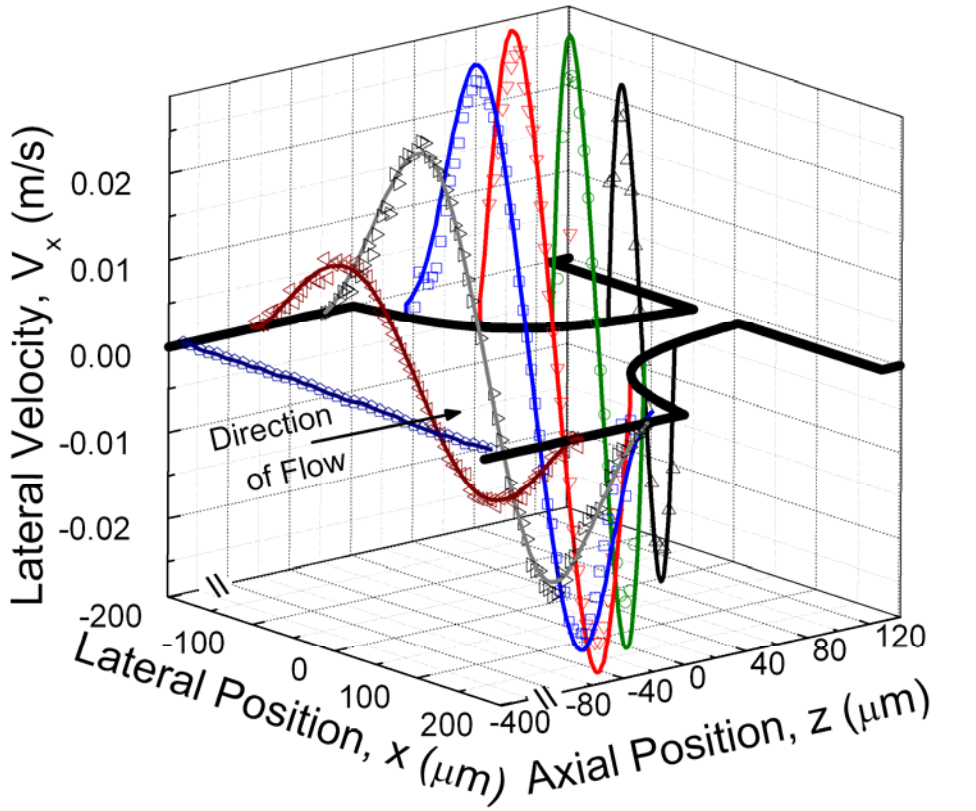

(b)

Fig. 4 Comparison of the velocity profiles at the center plane ($y = 0$) determined experimentally (open symbols) and numerically (solid lines), as a function of the axial and lateral positions for $Q = 1$ ml/h ($Re = 3.21$): (a) Velocity component in the z-axis direction; (b) Velocity component in the x-axis direction.

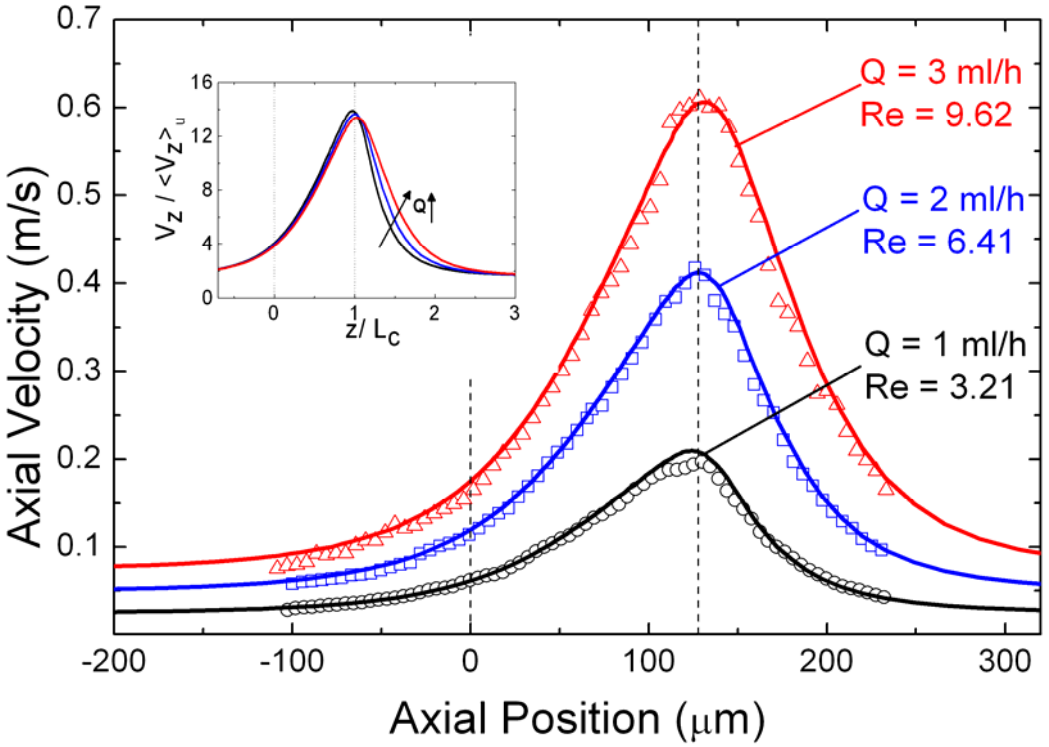

(a)

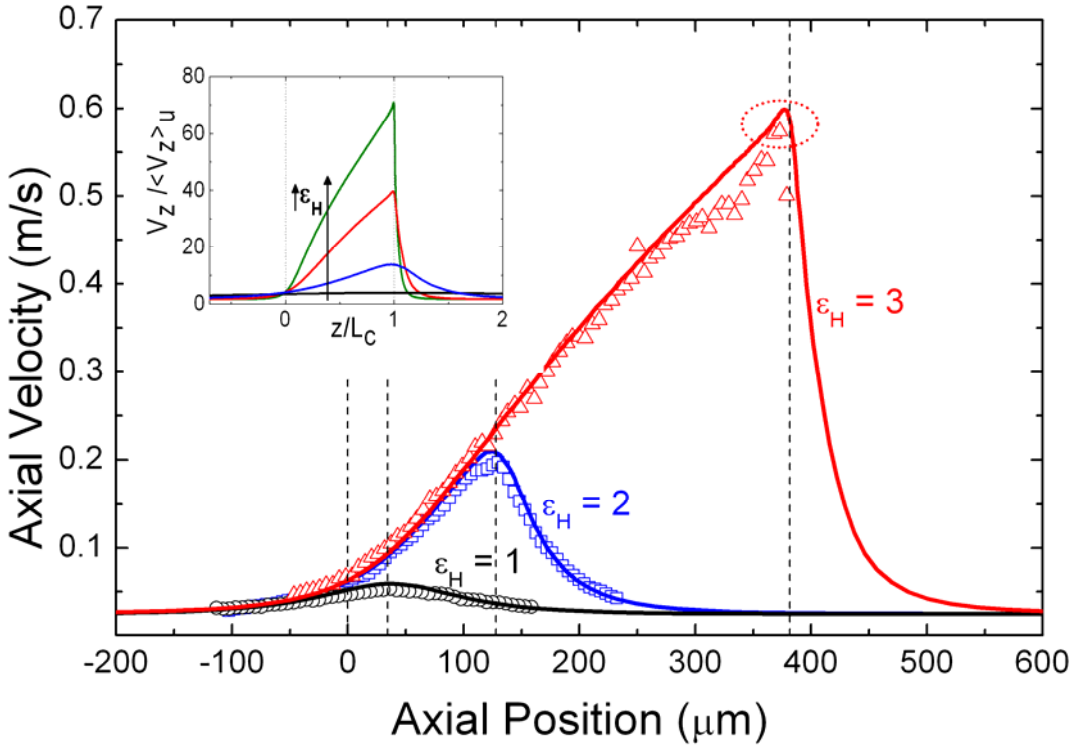

(b)

Fig. 5 Axial velocity profile along the centerline ($y = 0$, $x = 0$) measured experimentally (open symbols) and calculated numerically (solid lines). (a) Effect of flow rate at a fixed total Hencky strain, $\varepsilon_H = 2$; (b) Effect of the total Hencky strain at a fixed flow rate $Q = 1$ ml/h ($Re = 3.21$).The inset shows numerical results at Hencky strains of 1, 2, 3 and ln(40). The dashed vertical lines indicate the beginning and end of the contraction sections.

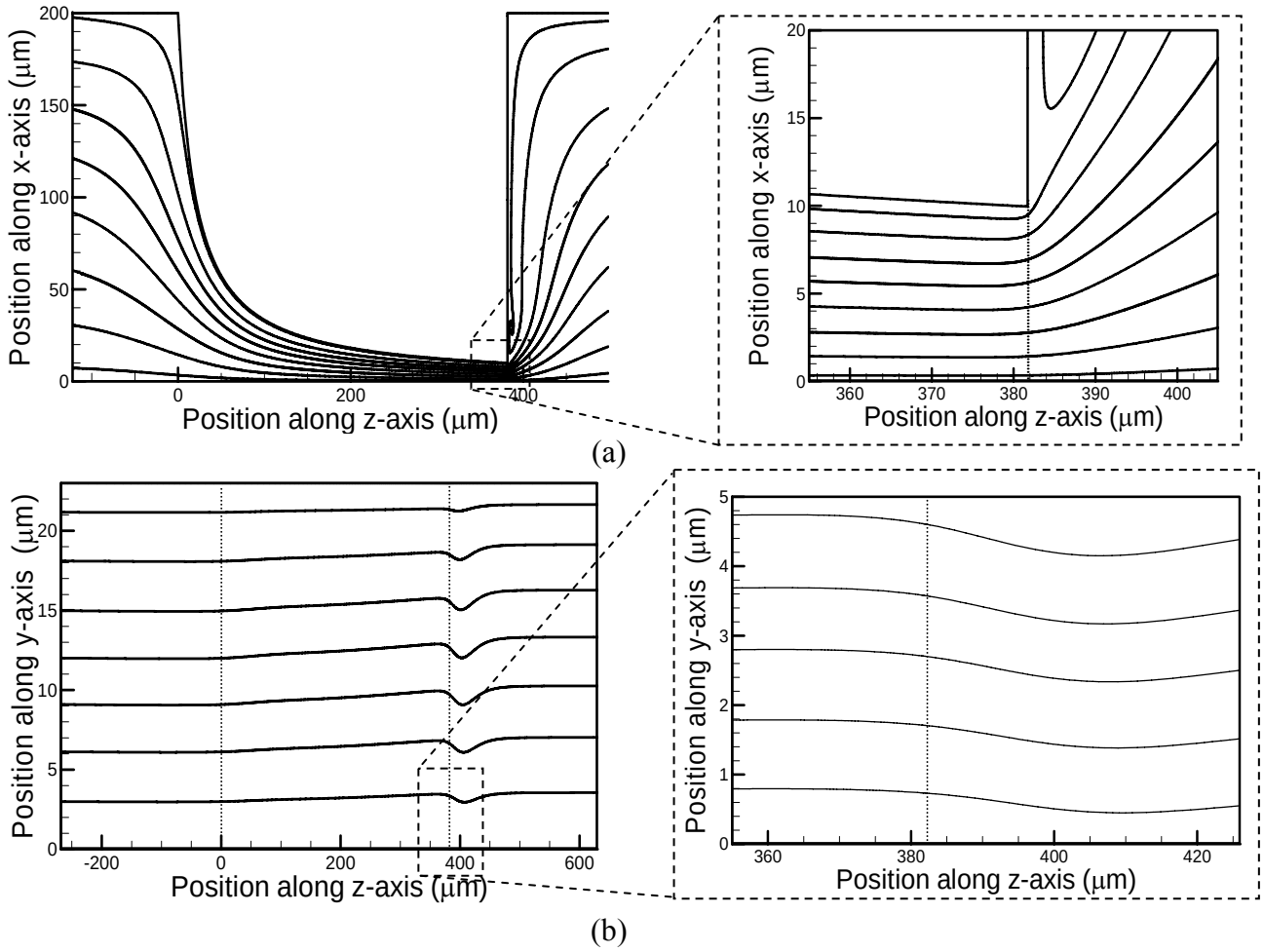

Fig. 6 Predicted streaklines for $\varepsilon_H = 3$ and $Q = 1$ ml/h ($Re = 3.21$): (a) at the center plane ($y = 0$); (b) at the z-y plane with $x = 0$. The vertical light lines mark the beginning and end of the contraction. Note that the axes are not to scale.

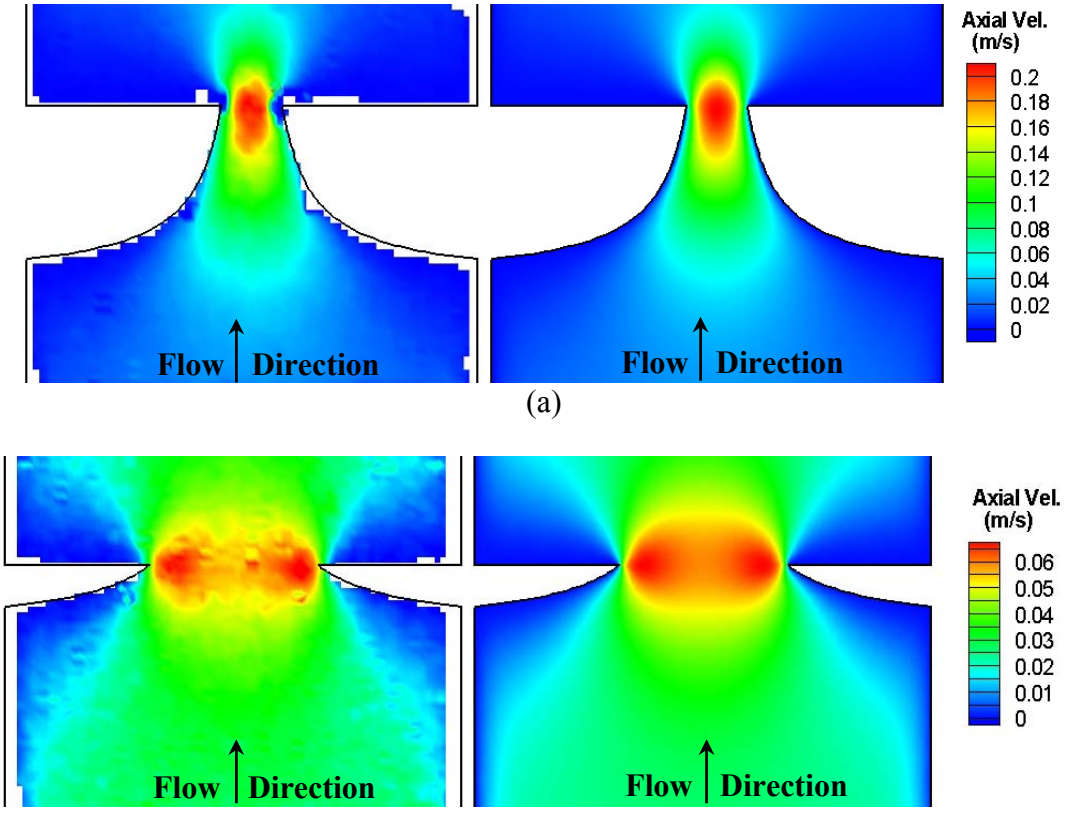

Fig. 7 Axial velocity contour plots at the center plane ($y = 0$) at $Q = 1$ ml/h ($Re = 3.21$). Comparison between experimental measurements (left) and numerical predictions (right) for: (a) $\varepsilon_H = 2$; (b) $\varepsilon_H = 1$.

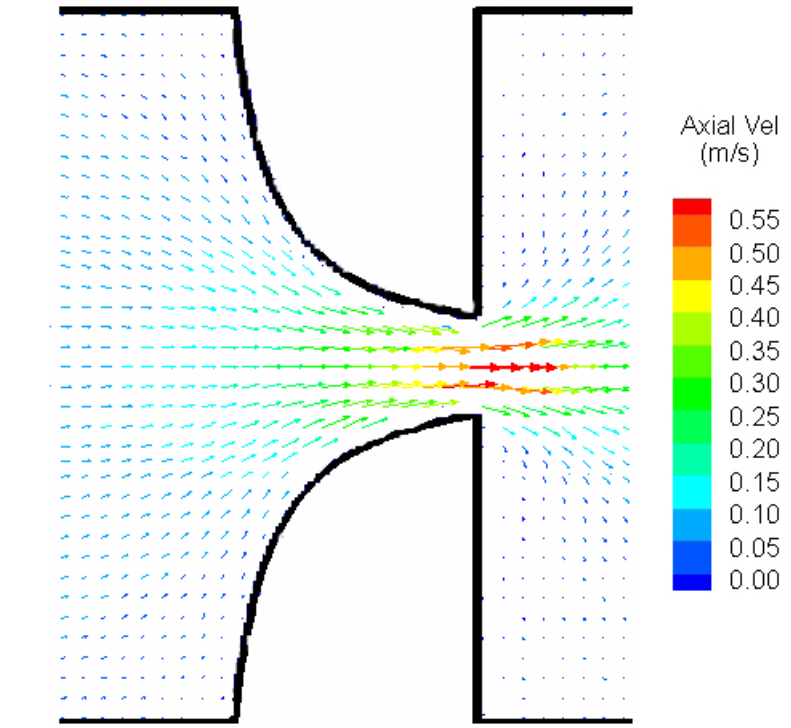

(a)

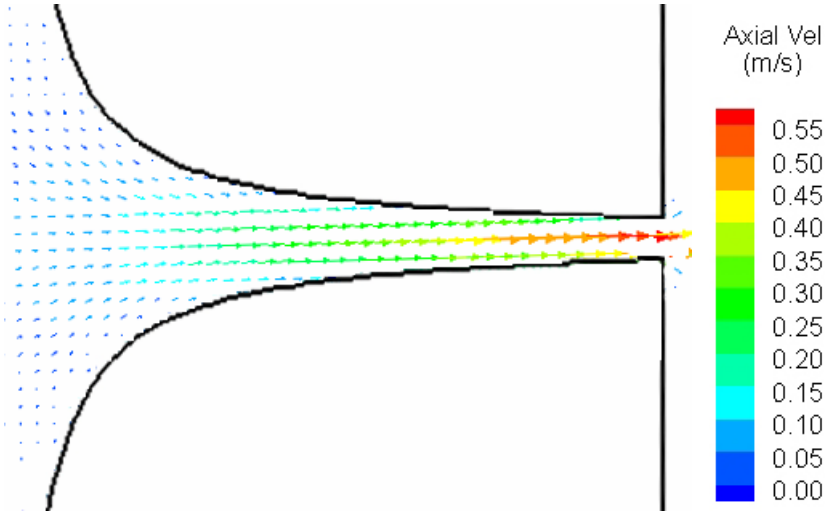

(b)

Fig. 8 Experimental velocity vector maps at the center plane ($y = 0$): (a) $Q = 3$ ml/h ($Re = 9.62$) and $\varepsilon_H = 2$ (b) $Q = 1$ ml/h ($Re = 3.21$) and $\varepsilon_H = 3$. For clarity, only a quarter of the total number of vectors are shown.

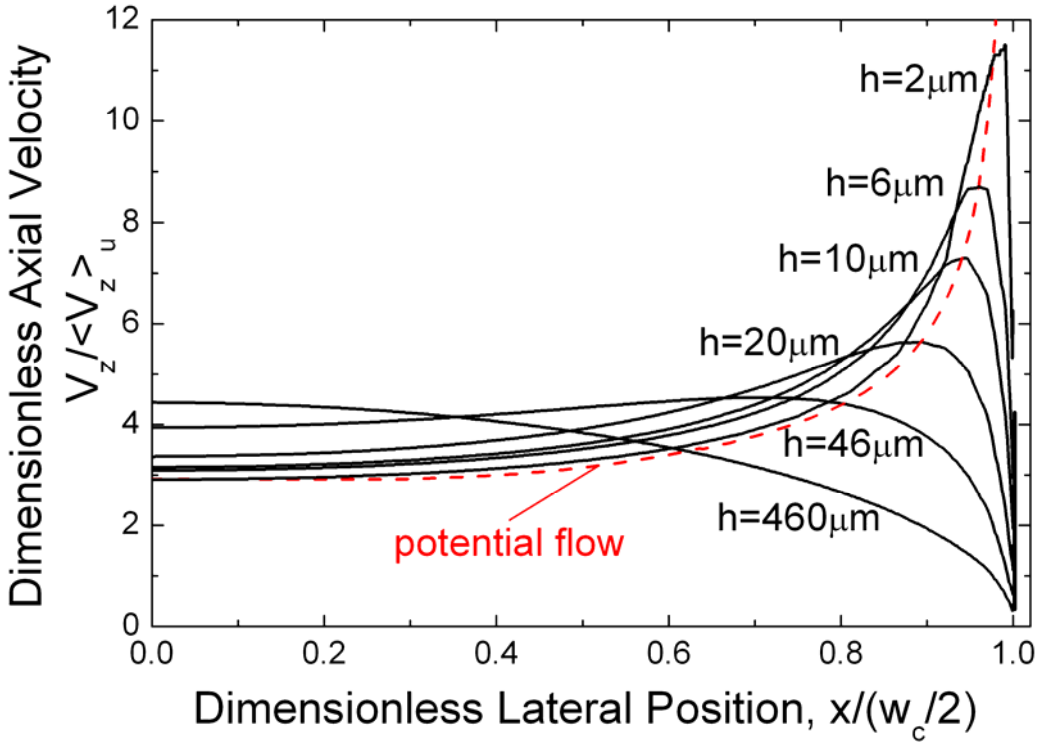

Fig. 9 Axial velocity profiles predicted numerically under creeping flow conditions at the intersection between the center plane ($y = 0$) and the expansion plane ($z = 34.4$ μm) for $\varepsilon_H = 1$ and a range of depths $4 \leq h \leq 460$ μm.

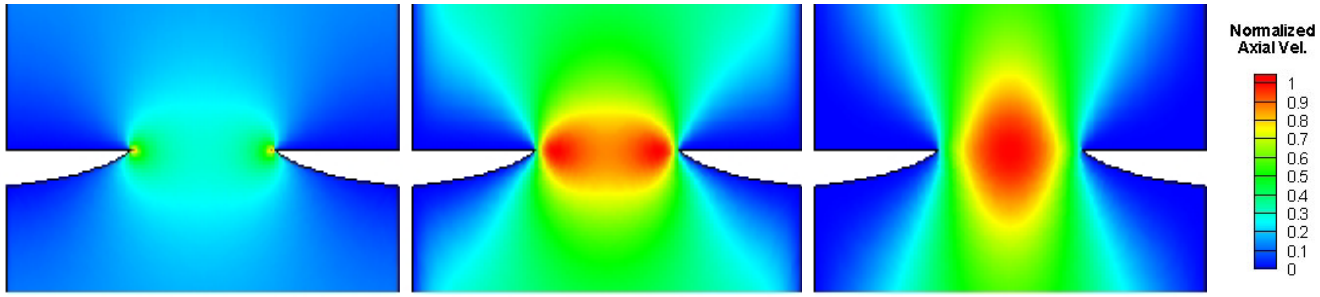

h = 4.6 μm h = 46 μm h = 460 μm

(a)

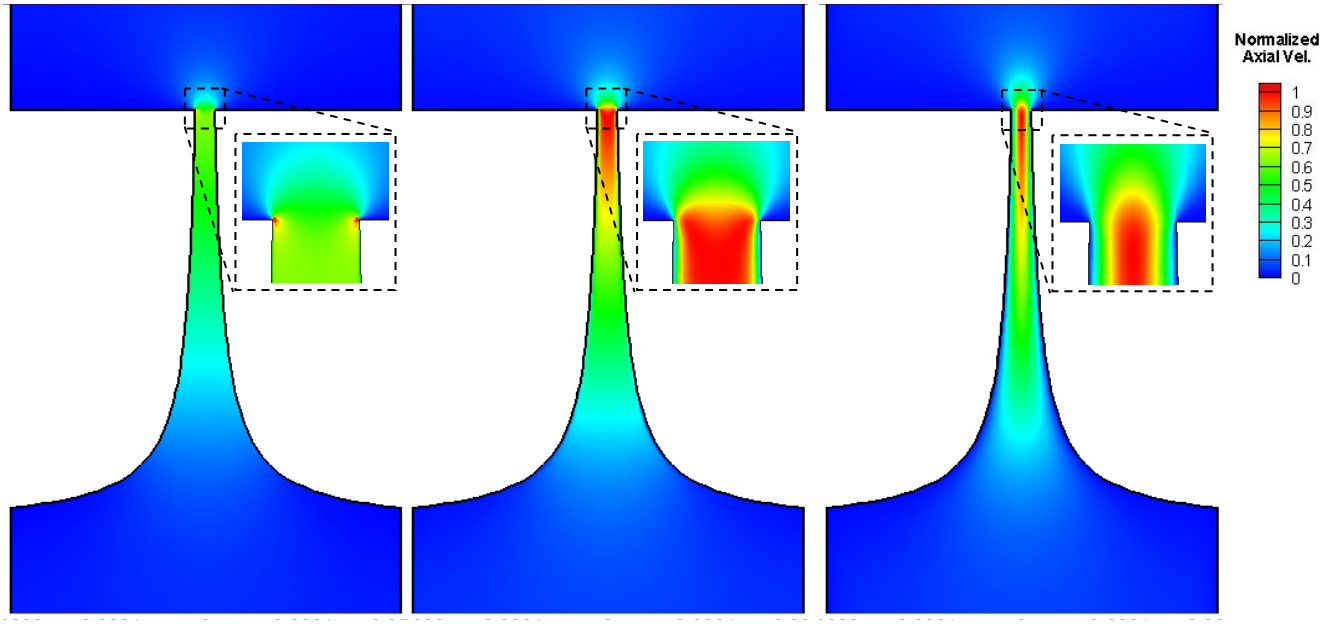

h = 0.46 μm h = 4.6 μm h = 46 μm

(b)

Fig. 10 Numerical contour plots of the normalized axial velocity (V_z /$V_{z,max}$) at the center plane (y = 0) obtained under creeping flow conditions for (a) $\varepsilon_H = 1$ and (b) $\varepsilon_H = 3$.

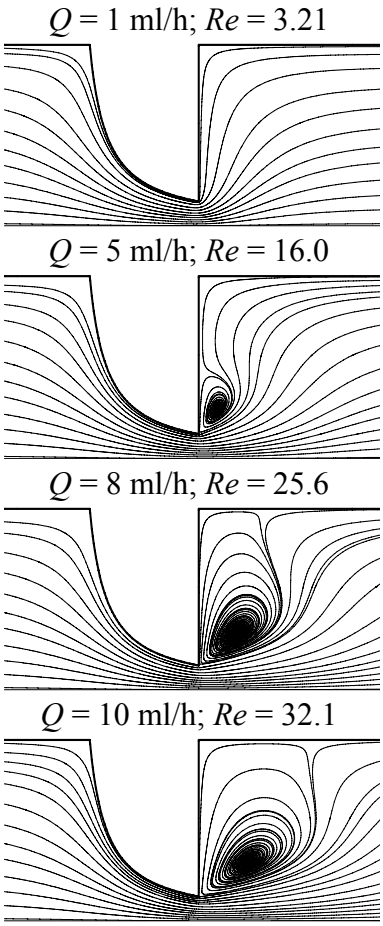

Fig. 11 Numerically predicted streaklines at the center plane ($y = 0$) for $\varepsilon_H = 2$ and increasing flow rates.

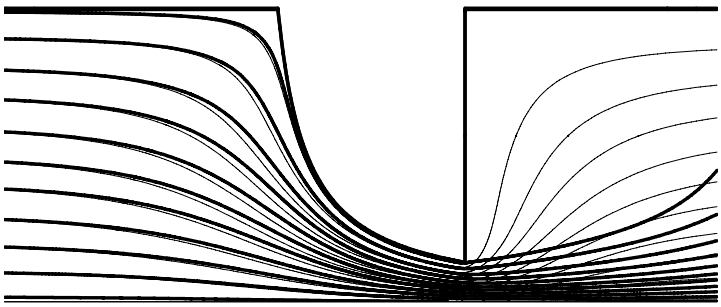

Fig. 12 Predicted streaklines for $\varepsilon_H = 2$: Q = 1 ml/h, Re = 3.21 (thin lines); Q = 10 ml/h, Re = 32.1 (thick lines).

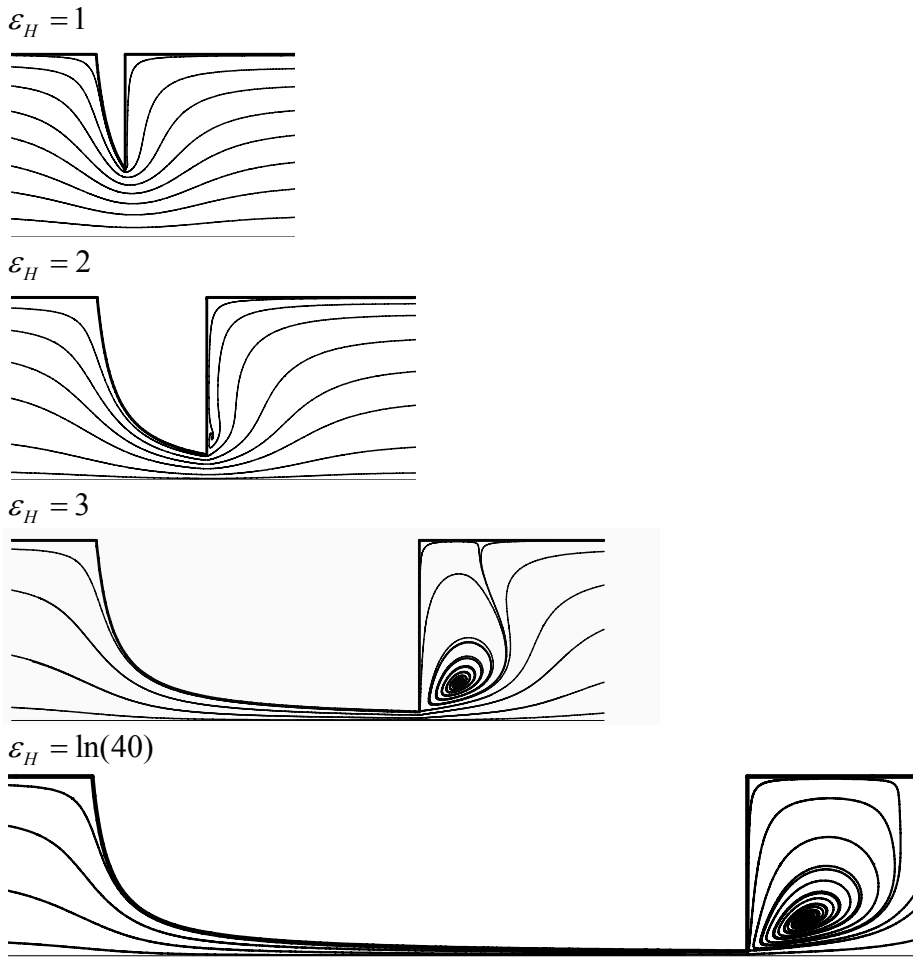

Fig. 13 Numerically predicted streaklines at the center plane ($y = 0$) for Re = 9.62 (Q = 3 ml/h) and four different Hencky strains.

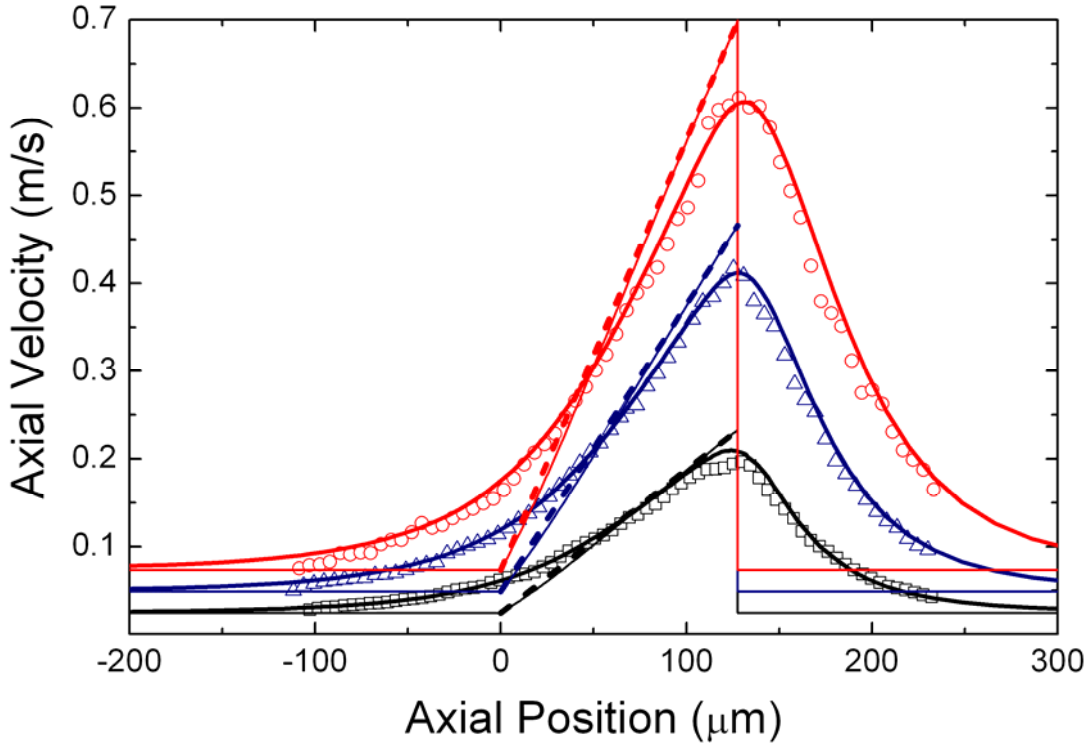

(a)

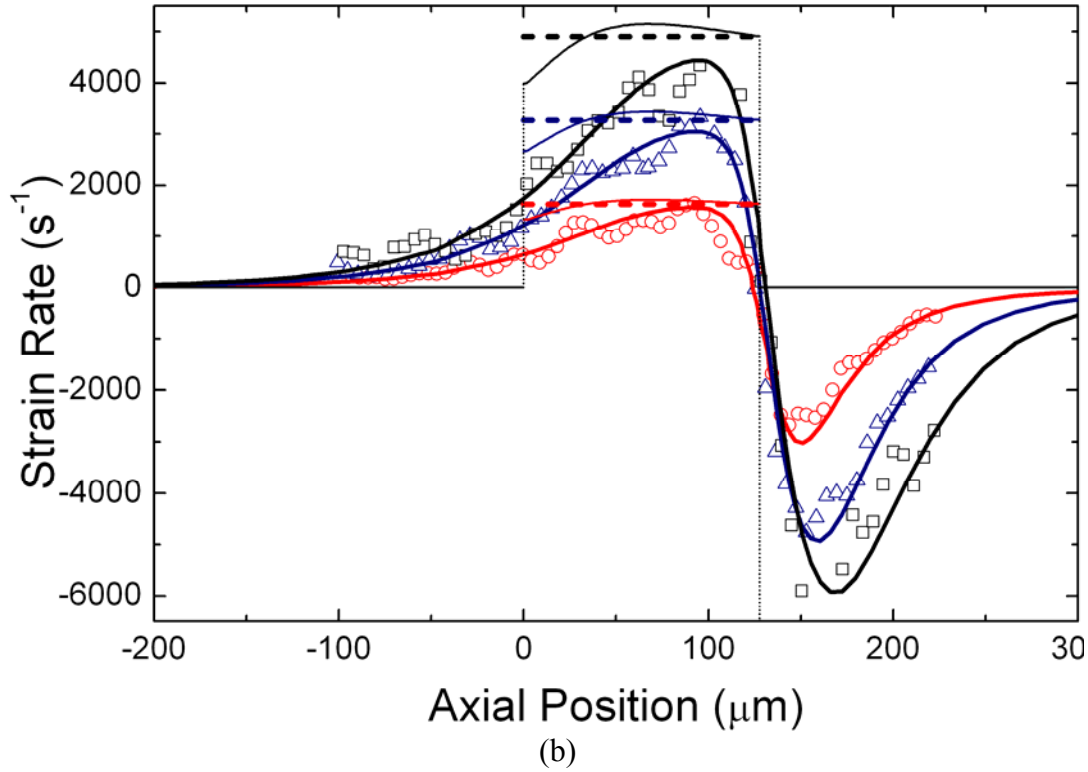

(b)

Fig. 14 Velocity profiles (a) and strain rate profiles (b) along the centerline for $\varepsilon_H = 2$: $Q = 1$ ml/h, $Re = 3.21$ (□); $Q = 2$ ml/h, $Re = 6.41$ (△) and $Q = 3$ ml/h, $Re = 9.62$ (○). The symbols correspond to experimental data, the thick lines to data from numerical predictions, the thin lines to the hypothetical fully developed case (equation 6) and the dashed lines to the ideal case with a linear variation between the contraction entrance and exit (equation 7).

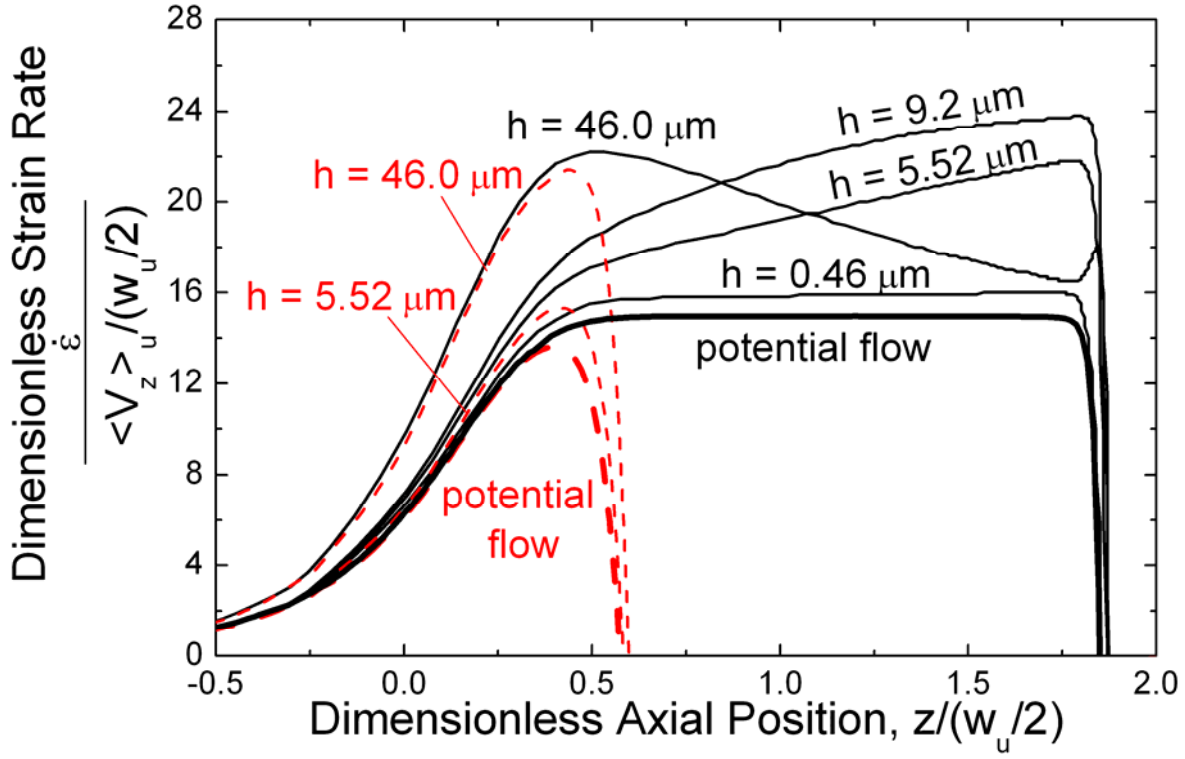

Fig. 15 Strain rate profiles along the centerline under creeping flow conditions for $\varepsilon_H = 2$ (dashed lines) and $\varepsilon_H = 3$ (solid lines).

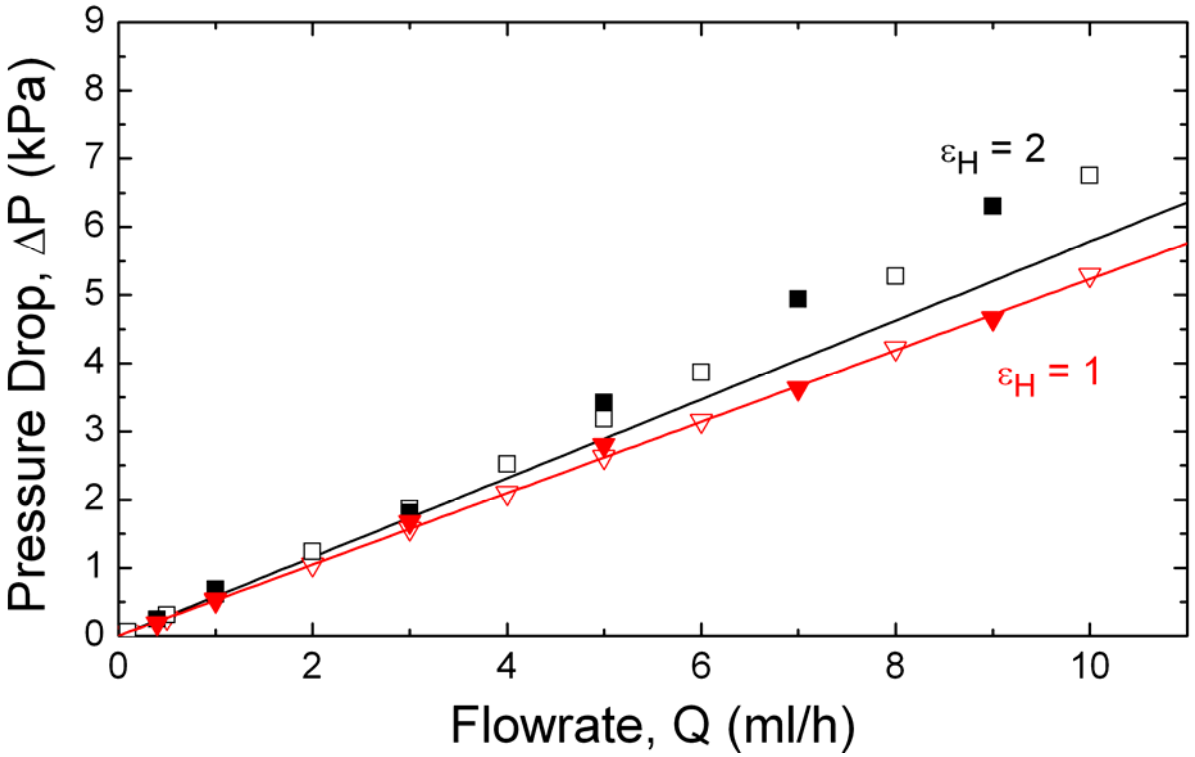

Fig. 16 Effect of flow rate on the total pressure drop determined experimentally (open symbols) and numerically (closed symbols) for $\varepsilon_H = 1$ and 2. The solid lines correspond to hypothetical pressure drops if there were no entrance or exit effects and assuming the flow is fully-developed everywhere.